Multimedia Tools and Applications (2025) 84:32643–32669
https://doi.org/10.1007/s11042-024-20370-0

Design of automatic follicle detection and ovarian classification system for ultrasound ovarian images

R. Saranya[1] **· R. Sridevi**[2]

Received: 24 April 2023 / Revised: 3 September 2024 / Accepted: 4 October 2024 /
Published online: 18 December 2024
© The Author(s), under exclusive licence to Springer Science+Business Media, LLC, part of Springer Nature 2024

Abstract
Polycystic Ovary Syndrome (PCOS) is a common reproductive and metabolic disorder characterized by an increased number of ovarian follicles. Accurate diagnosis of PCOS requires detailed ultrasound imaging to assess follicles' size, number, and position. However, noise often needs to be improved on these images, complicating manual detection for radiologists and leading to potential misidentification. This paper introduces an automated diagnostic system for integration with ultrasound imaging equipment to enhance follicle identification accuracy. The system consists of two main stages: preprocessing and follicle segmentation. Preprocessing employs an adaptive Frost filter to reduce noise, while follicle segmentation utilizes a region-based active contour combined with a modified Otsu method. Unlike the conventional Otsu method, where the threshold value is selected manually, the modified Otsu method automatically selects initial threshold values using an iterative approach. After segmentation, features are extracted from the segmented results. An SVM classifier then categorizes the ovarian image as normal, cystic, or polycystic. Experimental results demonstrate that the proposed method's Follicle Identification Rate is 96.3% and the False Acceptance Rate is 2%, which significantly improves classification accuracy, highlighting its potential advantages for clinical application.

Keywords Follicle · Biomedical instrumentation · Ultrasound image · Active contour · Modified Otsu · Sensing systems · Accuracy · Detection of PCOS

✉ R. Saranya
saranya_r@psgcas.ac.in

R. Sridevi
Sridevi.r@christuniversity.in

[1] Assistant Professor, Department of Computer Science with Data Analytics, PSG College of Arts & Science, Coimbatore, Tamil Nadu, India

[2] Associate Professor, Department of Computer Science, CHRIST University, Bangalore, Karnataka, India

1 Introduction

Today, one of the major issues concerned with endocrine disorders in women's health is Polycystic Ovary Syndrome, which affects 1 in 15 women worldwide and is a major financial health trouble that is likely to increase together with obesity, diabetes, and heart diseases [1]. This disorder exists in the ovary due to follicular cyst formation that obstructs the balance of follicle-stimulating hormones and luteinizing hormones. These hormones help eggs mature properly inside the ovaries. The accumulation of incompletely developed follicles leads to PCOS, which has common symptoms like irregularity in the menstrual cycle and an increase in weight that results in obesity, skin problems, undesired hair growth, and hyperinsulinemia [2–8]. Ultrasound is mainly used to image the uterus because of its noninvasive nature and attractive performance on soft tissues. During the image acquisition phase, speckle noise is introduced in the ultrasound image mainly due to the air gap between the human body and the transducer probe, though the gel is applied to reduce the air gaps [7]. An image's resolution and quality are highly dependent on the frequency range and the transducers used in the probe.

Speckle noise is multiplicative, which makes the diagnosis difficult by degrading the edges and the smallest discernible detail in an image. As a result of poor-quality images, misinterpretation of PCOS is possible. This necessitates efficient techniques to enhance the image and segregate the follicles in an ovary from noise. After segregating, PCOS disorder is identified based on the number of follicles and their size. Both normal ovaries and polycystic ovaries have follicles [8]. A standard criterion has been put forth by the American Society for Reproductive Medicine and the European Society of Human Reproduction and Embryology to differentiate polycystic ovary from normal ovary. These societies describe that ovaries with follicles 2.0–9.0 mm in size and follicle count of 12 or higher are classified as polycystic ovaries. A radiologist using a conventional ultrasound machine to scan the ovary rotates the probe progressively to recognize the follicle and measure its dimension. This manual detection is time-consuming and painful to the patient. In order to overcome the problems during image capturing and manual detection, this paper proposes an automatic diagnostic system with a denoising filter and segmentation algorithm.

2 Literature review

In the literature, several methods for speckle noise reduction have been proposed. Denoising techniques based on wavelet threshold are effective and do not degrade the sharpness of the regions in the image but have high computational cost [9–13]. Michailovich et al. introduced a de-speckling method to avoid disturbing the anatomical content of the image [14]. To detect gray areas from dermoscopic images, Sforza et al. proposed an adaptive thresholding technique that accurately detects gray areas [15]. Delsanto et al. proposed an automatic segmentation algorithm for carotid artery segmentation. The segmentation results are analyzed using a medical expert's manual segmentation results [16]. Gao et al. introduced an optimal thresholding method using quantum-behaved particle swarm optimization for image segmentation [17]. Region-growing methods are less noise-sensitive and increase the recognition rate [18]. A better recognition rate was achieved when parametric evaluation and polynomial filtering techniques were applied to medical images [19–21]. Giordano et al. proposed an efficient image preprocessing technique for automatic bone age evaluation [22]. Osowski et al.

introduced GA and SVM for blood cell recognition [23]. Berahmand, K., Daneshfar, F., Salehi, E.S. et al. surveyed various auto-encoder algorithms used in machine learning algorithms [24]. Berahmand, K., Daneshfar, F., Salehi, E.S. et al. developed a new algorithm by combining the Crow algorithm and a decision tree to detect Parkinson's disease, which provides efficient results [25]. Casciaro et al. solved enhancement problems using multi-frequency differential filtering [26]. Chan and Vese introduced the active contours method and considered information inside the region using level-set methods [27]. Zhang et al. (2017) utilized a median filter to remove speckle noise in ultrasound images, which is vital for preserving the clarity of ovarian follicles. Kumar and Gupta (2018) utilized wavelet-based denoising techniques to enhance the quality of ultrasound pictures of the ovary. The research showed a significant increase in signal-to-noise ratio yet preserved important features [28]. Rajan et al. (2016) employed histogram equalization to improve the contrast of ultrasound images. This method has made it more visible that ovarian cysts assist with better diagnosis [29]. Li and Zhou (2019) used contrast-limited adaptive histogram equalization on ultrasound images of ovaries. Their outcomes show improved visibility of subtle structures, which is critical in the accurate detection of cysts [30]. Canny edge detection was employed by Bhattacharya et al. 2016 where they targeted at detection of the edges of ovarian cysts appearing in ultrasound images Wang et al. (2018) [31]. Intensity normalization techniques for standardizing pixel intensity values across various ultrasound images, thus minimizing variability and enhancing consistency in subsequent steps involved in image analysis while applying Otsu's thresholding technique for segmentation of ovarian cysts from ultrasound images [32]. This study illustrated how this method could help distinguish cysts from neighboring tissues according Personalized diagnostic algorithm for women with PCOS [33].

Consequently, the approach dynamically adjusted the cutoff level based on the neighboring pixels' properties to attain more accurate and precise cyst segmentation results. Region-growing techniques to segment ovarian follicles in their study [34]. In their method, a region was grown from an initial seed point until certain features were met; this way, they could accurately outline ovarian cyst borders [35]. The watershed segmentation technique was used when dealing with ultrasound images of cysts. This technique can address cases with overlapping regions of neighboring cysts [36]. While this effectively outlines [37–41] the contours of simple cystic masses, it may not be appropriate for complex ovarian structures like dermoids or endometriomas with internal echoes that can also be detected [35, 42–44].

3 Method

The functional blocks of the proposed automatic diagnostic system are shown in Fig. 1. To deal with medical images, we have to carefully choose the steps. Naturally, ultrasound ovarian images are prone to noise, so preprocessing is necessary. A step is carried out to detect the follicle segmentation. From the segmented output, features are extracted, which are needed for classification. The automatic detection system for ovarian follicles in ultrasound images involves several key stages: input image acquisition, preprocessing, Region of Interest (ROI) extraction, speckle noise removal, follicle identification, feature extraction, and classification.

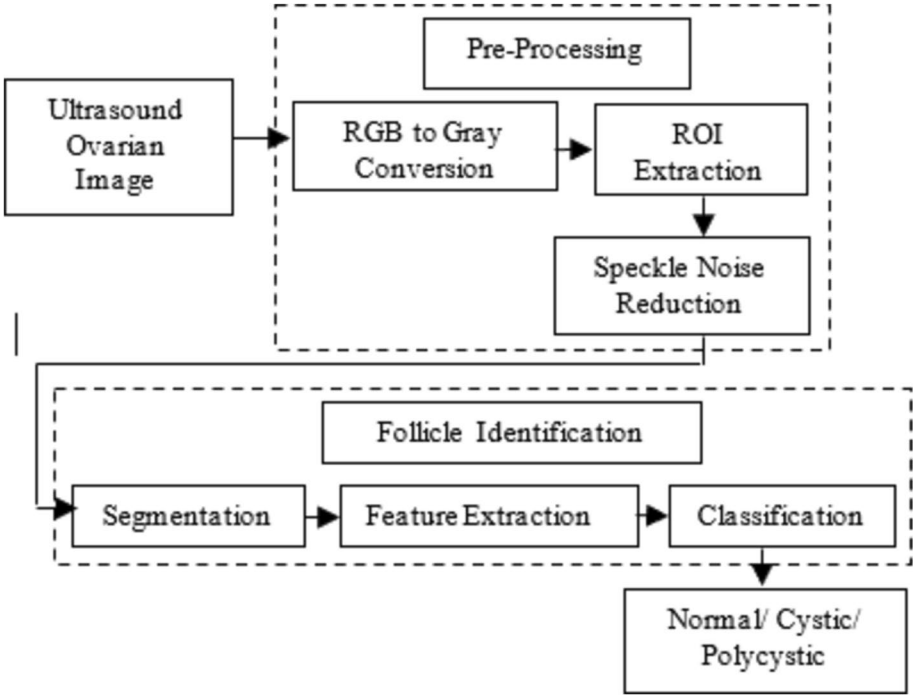

Fig. 1 Block diagram of automatic detection of ovarian follicles in Ultrasound Images

Input image acquisition The system begins with capturing high-resolution ultrasound images of the ovaries. These images serve as the primary input for the entire detection process.

Preprocessing In the preprocessing stage, the ultrasound image undergoes initial enhancements to prepare it for analysis. Since the ovary occupies a small region within the ultrasound image, extracting the Region of Interest (ROI) is crucial. This step isolates the ovary from the rest of the image, ensuring that subsequent processing focuses only on the relevant area.

ROI extraction The ROI extraction process involves identifying and isolating the ovary from the ultrasound image.

Speckle noise removal Ultrasound images are often affected by speckle noise, which can obscure important details. Various speckle filtering techniques, such as an adaptive Frost filter to reduce noise, are employed to reduce this noise while preserving the edges and fine details of the ovarian structures.

Follicle identification In the follicle identification phase, the follicles within the ovary are segmented using a proposed hybrid method to accurately delineate the follicles. This part utilizes a region-based active contour combined with a modified Otsu method. Unlike the conventional Otsu method, where the threshold value is selected manually, the modified Otsu method automatically selects initial threshold values using an iterative approach.

Table 1 Performance Metrics

MSE	$MSE = \frac{1}{CK}\sum_{s=1}^{C}\sum_{k=1}^{K}(D(s,k) - D'(s,k)^2$
PSNR	$PSNR = 10\log\frac{255^2}{MSE}$
NK	$NK = \sum_{s=1}^{C}\sum_{k=1}^{K} D(s,k)D'(s,k) / \sum_{s=1}^{C}\sum_{k=1}^{K} D^2(s,k)$
AD	$AD = \sum_{s=1}^{C}\sum_{k=1}^{K}\big(D(s,k)D'(s,k)\big)/CK$
SC	$SC = \sum_{s=1}^{C}\sum_{k=1}^{K} D^2(s,k) / \sum_{s=1}^{C}\sum_{k=1}^{K} D'^2(s,k)$
MD	$MD = Max\big(\lvert D(s,k) - D'(s,k)\rvert\big)$
NAE	$NAE = \sum_{s=1}^{C}\sum_{k=1}^{K} \lvert D(s,k) - D'(s,k)\rvert / \sum_{s=1}^{C}\sum_{k=1}^{K} \lvert D(s,k)\rvert$

Feature extraction Once the follicles are segmented, geometric features such as size, shape, perimeter, and area are extracted from the segmented regions. These features are critical for differentiating between normal, cystic, and polycystic ovaries.

Classification The extracted features are then fed into a classification algorithm, which could be a machine learning model support vector machine. The classifier analyzes the features and categorizes the ovary as normal, cystic, or polycystic.

Automatic diagnostic systems using ultrasound images produce less accurate results due to speckle noise, also called multiplicative noise [14]. Table 1 shows the different performance metrics used to evaluate the filters' performance.

Recent advances in the automation of medical diagnosis using ultrasound imaging systems necessitate efficient de-noising techniques for removing speckle noise. For denoising, Lee, Kuan, Frost, Median, Gaussian and Wiener filtering techniques are applied on ovarian images and their performances are evaluated using specific metrics and metrological indicators, namely, Mean Square Error (MSE), Maximum Difference (MD), Peak Signal to Noise Ratio (PSNR), Normalized Cross Correlation (NK), Normalized Absolute Error (NAE), Absolute Difference (AD), and Structural Content (SC). In the equations, D represents the original ultrasound ovary image, $^{and\ D}$ denotes the noise-free image. Then, C and K represent, respectively, the number of rows and columns in an image. Based on the performance study, this paper proposes an adaptive Frost filter approach to de-noise ultrasound ovary images for accurate segmentation.

4 Proposed adaptive frost filter

This proposed adaptive Frost filter is a hybridization of a Wiener filter and a Frost filter for de-noising. It improves the quality of the ovary image for accurate segmentation. The Wiener filter removes the blurring in the image, and then the resulting image is convolved with a spatially varying Frost kernel [26–29] described in Eq. (1).

$$\overline{K}(d,e) = g_1(d,e) \bullet m_1(d,e) \tag{1}$$

where $g_I(d, e)$ is the input image and the kernel $m_I(d, e)$, centred at the pixel at location.

Figure 2(a) shows an input ovarian image. Figure 2 (b)–(d) gives a visual assessment of the proposed adaptive Frost-filtered images with better speckle noise suppression. In Appendix: Figs. 8, 9, 10, 11, 12, 13, and 14, filters of different kernel sizes are taken on the x-axis, and the performance metric is taken on the y-axis. Kernel sizes of 3×3,

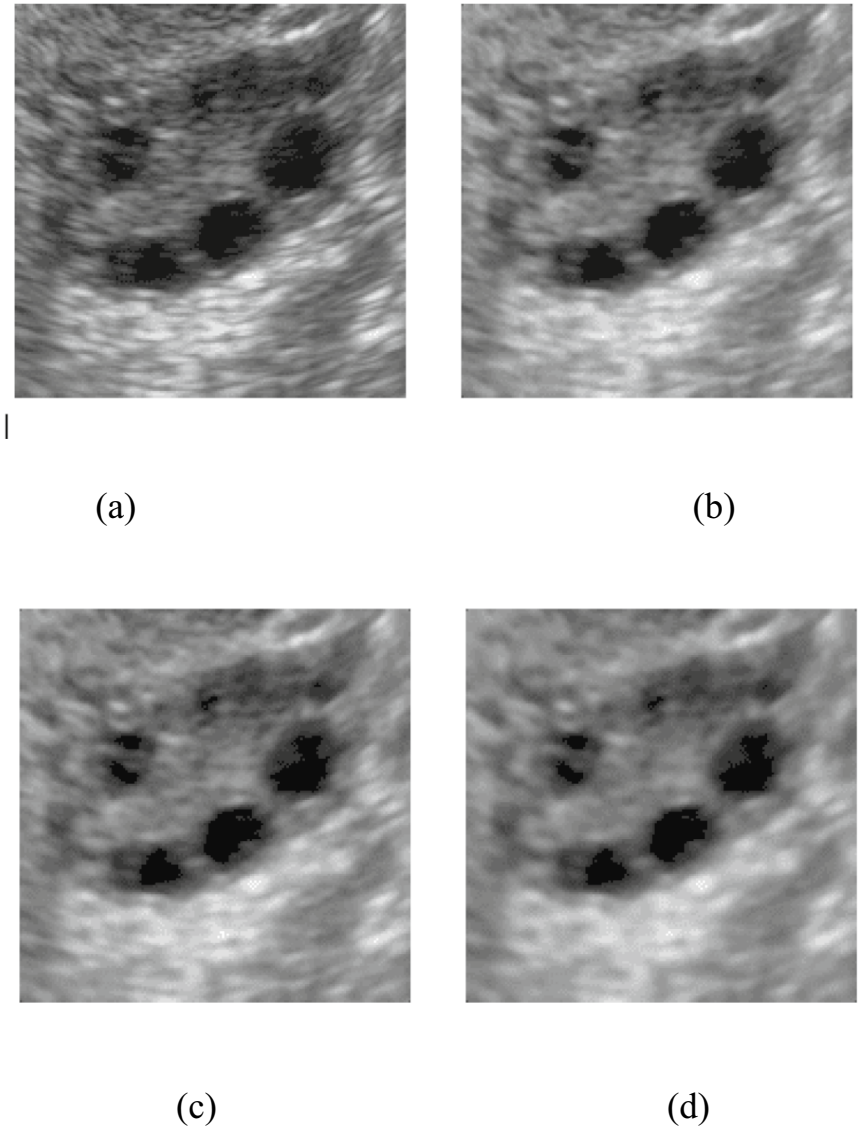

Fig. 2 **a** Input ovarian image (**b**) Proposed adaptive frost 3×3 (**c**) Proposed adaptive frost 5×5 (**d**) Proposed adaptive frost 7×7

Table 2 Performance metrics of different de-noising filters for image I

Filters	Window Size /Frequency	Performance Metrics						
		AD	MD	MSE	NAE	NK	PSNR	SC
Proposed Adaptive Frost P3	3×3	0.027	58.000	**116.473**	**0.097**	0.981	**27.468**	**1.024**
Proposed Adaptive Frost P5	5×5	0.060	66.000	165.854	0.116	0.974	25.933	1.033
Proposed Adaptive Frost P7	7×7	0.094	69.000	208.734	0.129	0.969	24.934	1.040
Frost F3	3×3	0.022	65.000	174.894	0.118	0.976	25.703	1.028
Frost F5	5×5	0.050	80.000	236.234	0.138	0.968	24.397	1.039
Frost F7	7×7	0.081	79.000	282.952	0.151	0.961	23.613	1.047
Lee L3	3×3	0.001	73.000	187.224	0.122	0.975	25.407	1.029
Lee L5	5×5	-0.002	83.000	265.126	0.147	0.965	23.896	1.042
Lee L7	7×7	-0.001	89.000	330.623	0.164	0.957	22.937	1.052
Kuan K3	3×3	0.373	216.000	233.079	0.129	0.970	24.455	1.035
Kuan K5	5×5	0.398	263.000	248.023	0.148	0.965	22.308	1.053
Kuan K7	7×7	0.401	288.000	266.056	0.177	0.994	21.037	1.060
Median M3	3×3	1.529	133.000	268.206	0.141	0.951	23.846	1.072
Median M5	5×5	1.521	133.000	268.206	0.141	0.951	23.846	1.072
Median M7	7×7	1.529	133.000	268.206	0.141	0.951	23.846	1.072
Wiener W3	3×3	**-0.005**	**41.000**	132.115	0.098	0.982	26.921	1.022
Wiener W5	5×5	0.065	54.000	166.946	0.120	0.974	25.905	1.034
Wiener W7	7×7	0.186	61.000	212.644	0.135	0.966	24.854	1.045
Gaussian G1	($f_c = 10$)	0.827	120.000	464.254	0.192	**0.928**	21.463	1.101
Gaussian G2	($f_c = 20$)	0.208	92.000	303.915	0.156	0.955	23.303	1.059
Gaussian G3	(fc = 30)	0.092	81,000	228.282	0.136	0.966	24.546	1.044
Optimum Value		**-0.005**	**41.000**	**116.473**	**0.097**	**0.928**	**27.468**	**1.024**

5×5, and 7×7 are used in Lee, Kuan, Frost, Median, and Wiener filters as well as in the proposed filter. Gaussian low pass filters use 10, 20, and 30 Hz cut-off frequencies. In this work, we have taken a database of 63 ovary images. Due to space constraints, the experimental results of three ultrasound images, Image I, Image II, and Image III, are only presented in this manuscript. Table 2 provides additional results to observe the filter performance in terms of MSE, PSNR, NK, AD, SC, and MD for Image I. Minimizing the MSE, NAE, NK, SC, AD, and MD maximizing the PSNR values results in a better de-noising filter [35, 39–42]. The performance metrics are shown in Table 2, and the plots in Appendix: Figs. 8, 9, 10, 11, 12, 13, and 14, it can be inferred that the proposed adaptive Frost filter of 3×3 kernel size is de-noising better than all other filters. Gaussian, Lee, and Kuan filtering techniques blurred the image, and the Wiener filter successfully de-noised the image for a kernel size of 3×3. Lee filter failed to remove noise in the regions near the edges.

A Frost filter with a kernel size of 3×3 yielded a better peak signal-to-noise ratio. The proposed adaptive Frost filters are found to be high, and MSE, NAE, and SC are observed to be low. The proposed filter is found to have better performance and is hence chosen to denoise the ultrasound ovarian image for follicle segmentation.

5 Follicle segmentation

Segmenting follicles from ovary images is difficult due to the presence of soft tissue, ordinary tissue, and blood vessels. This section discusses the performance of the Otsu method and the proposed method for the segmentation of follicles from the ovary image. As discussed earlier, the denoised image is taken as an input for the follicle segmentation. The Otsu method binarizes the image into two groups to minimize within-class variance [31–45]. The result of the Otsu method is shown in Fig. 3. Figure 3 (a) An ultrasound ovary image with follicles. (b) The result is given by the conventional Otsu's method. (c) Area open image. (d) Result of the counted follicles. (e) Result of the edge detected image. (f) Overlaid on original image shows respectively.

Otsu's method does not produce satisfactory results in extracting follicles from ovary images. From the performance of the Otsu method, it is observed that a better segmentation method is needed to obtain accurate results. Hence, this paper proposes proficient segmentation techniques, namely the proposed modified Otsu method and the proposed hybrid method.

6 Proposed modified Otsu method

The idea of estimating the initial threshold [46, 47] value in the Otsu method using the iterative method is introduced here. Initially, the threshold T_1 is determined by computing the average value of the pixels in the ovary image. At the first iteration, the intensity of the

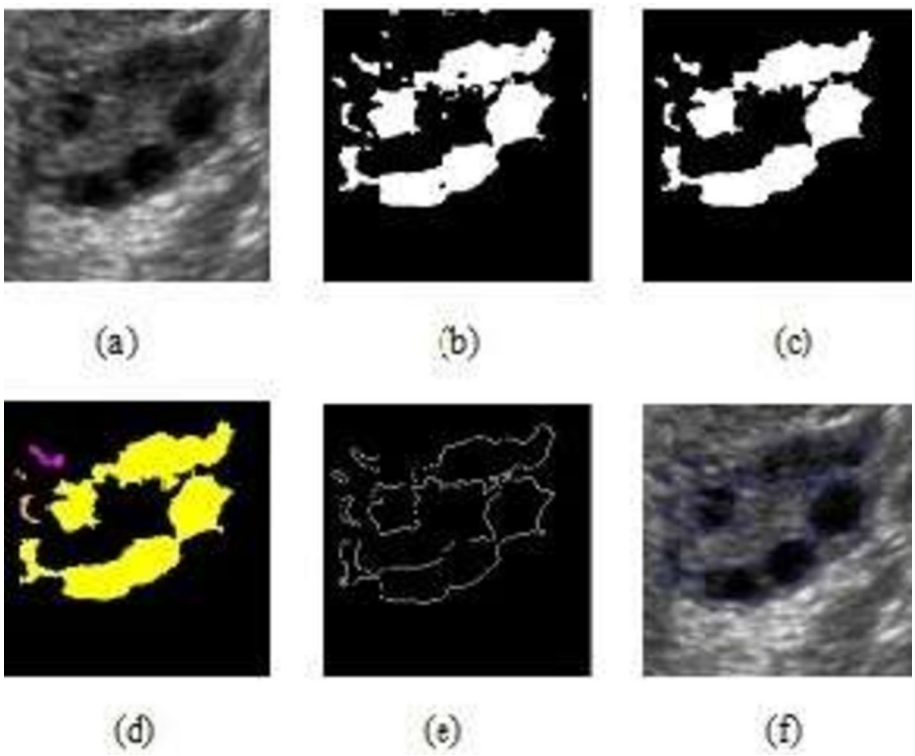

Fig. 3 Results of the conventional Otsu method

image, which is not less than the threshold T_1, is identified. In the next step, the mean of the intensity values above a current threshold value and the mean of the intensity values below the current threshold value are calculated and are denoted as $m_1^{[1]}$ and $m_2^{[1]}$, respectively, which is shown in Eq. 2.

The new set of thresholds is calculated as

$$T[1] = \frac{m_1^{[1]} + m_2^{[1]}}{2} \tag{2}$$

The newly calculated threshold value T [1] is carried forward to the next iteration. The superscript denotes the number of iterations. At the second iteration, the intensity of the image, which is not less than the current threshold T [1], is found. In the second iteration, the mean value $m_1^{[2]}$ below the current threshold T [1] and the mean value $m_2^{[2]}$ above T [1] is calculated. Similarly, the second iteration given in Eq. 3 calculates the threshold value as

$$T[2] = \frac{m_1^{[2]} + m_2^{[2]}}{2} \tag{3}$$

The iteration proceeds until the threshold value converges $T[K] - T[K-1]$. At the last iteration, the new threshold value is calculated using Eq. 4

$$t^{**} = \frac{m_1{}^{[K]} + m_2{}^{[K]}}{2} \tag{4}$$

The between-class variance given in Eq. 5. of the conventional Otsu method is defined as

$$\sigma_B^2(t) = K_1(\mu_{c_1} - \mu_t)^2 + K_2(\mu_{c_2} - \mu_t)^2 \tag{5}$$

K_1 and K_2 represent the probabilities of the two groups. Iteratively calculated threshold value t^{**} is now used as an initial threshold for the conventional Otsu method [45]. The μ_{c_1} ,μ_{c_2} are the means of two groups, and μ_t is the total mean calculated using Eq. 6 and Eq. 7.

$$\mu_{c_1}(t) = \sum_{j=1}^{t^{**}} \frac{j\,\mathrm{P}(j)}{K_1(t)\mu_{c_1}(t)} \tag{6}$$

$$\mu_{c_2}(t) = \sum_{j=t^{**}+1}^{S} \frac{j\,\mathrm{P}(j)}{K_2(t)} \tag{7}$$

The mean is calculated for the whole image and is given in Eq. (8).

Table 3 Otsu and proposed modified Otsu threshold for ultrasound ovary images

Image	Otsu threshold	Proposed Modified Otsu threshold
Image 1	37	29
Image 2	36	31
Image 3	43	34

$$\mu_t = \sum_{j=1}^{S} j \Pr(j) \tag{8}$$

The proposed modified Otsu method is applied to ultrasound ovary images. The results of the Otsu method and the proposed modified Otsu method are shown figures. Table 3 shows the threshold values obtained for the ovary images of these two methods. It is observed that there is only a small difference between the two threshold values. It can be noticed that there is a significant difference in identified follicles for the same image. Otsu method produces correct results only when the image histogram is bimodal. The proposed modified Otsu method produces accurate results for different types of histograms. The proposed modified Otsu method performs better for segmenting the follicles than the conventional Otsu method and almost matches human experts' manual prediction of follicles.

To further improve the accuracy of the automated segmentation process, this modified Otsu method is hybridized with a region-based active contour technique based on the Level Set Methodology, which is discussed below.

7 Proposed hybrid method

In the region-based active contour method, the initial contour can be placed anywhere in the image, and this contour initialization is a difficult task. Poor initialization can produce the contour away from the follicle region. The analogy to this, the Level Set method uses manual initialization of contour for segmentation [27–30]. This paper proposes a hybrid method for automatic extraction of follicles that combines the proposed modified Otsu method with region-based active contour [29–31].

The modified Otsu method produces the binary image consisting only of the background (zero) and object (white), which is used as a binary mask to initialize the contour position in the proposed hybrid method. Specifying the initial contour position closest to the preferred object boundaries is needed for accurate and faster diagnosis. The initial mask for the Level Set algorithm is shown in Fig. 4 (c), where C is represented as a level set of a function ϕ.

The zero-level set contour is represented as.

$$C = \{(y, z), \phi(y, z) = 0\}$$

Figure 4 (a) shows an Ovary image. (b) Histogram of an ovary image. (c) Proposed modified Otsu result. (d) The result is given by the proposed hybrid method. (e) The result of the identified follicles. (f) Edge detected image. (g) The result overlaid on a human expert's original image (h) Manual detection. The signed distance function is obtained from the initial mask. The narrow band approach reduces the computation time taken by the Level Set method to make a ϕ change [28–31]. Values of the ϕ are updated to exist within the narrow band. Narrowband curves are given by Eq. 9.

$$C_{nb} = \{(k, l) - \beta_0 \leqslant \beta_0, k = [0, i-1], l = [0, j-1]\} \tag{9}$$

where k, l is represented as pixel coordinates and i, j represents the height and width of ϕ.

The mean curvature of the level set function is given by the Eqs. 10,

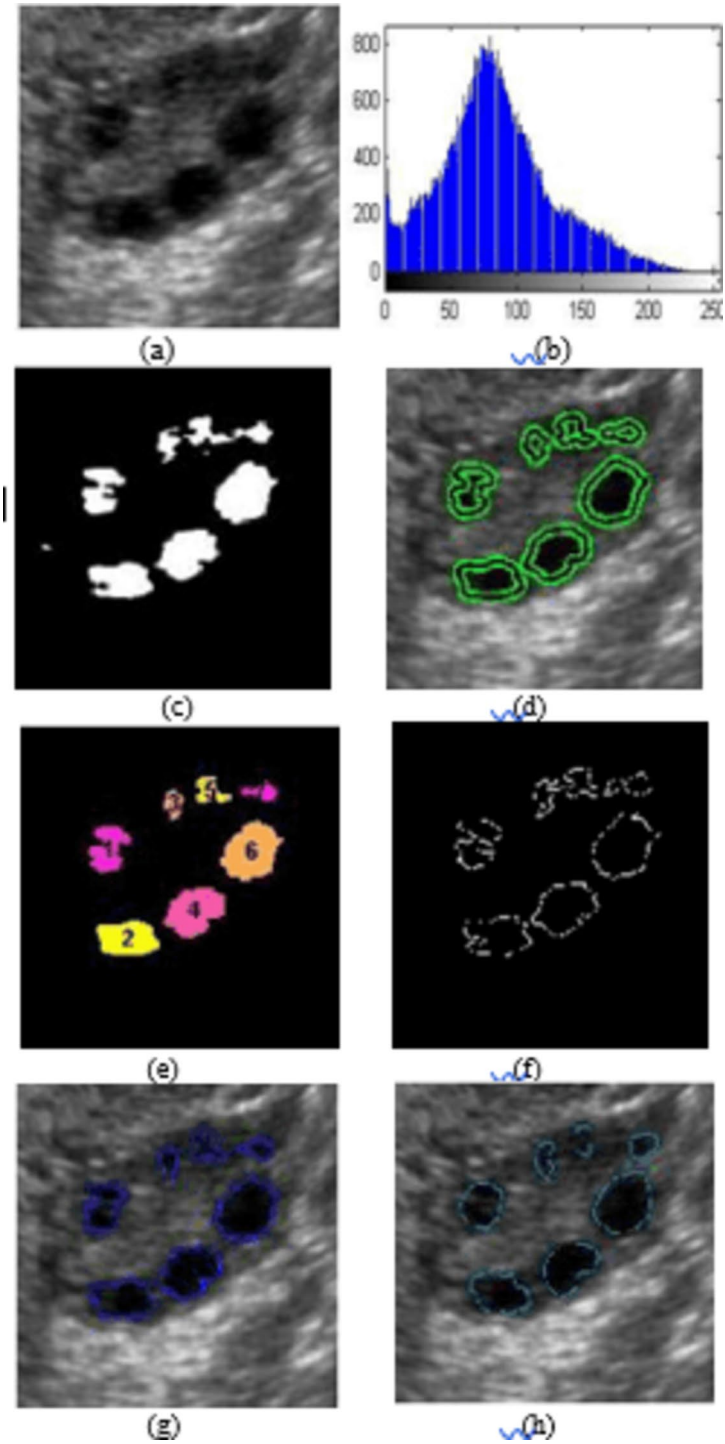

Fig. 4 Segmentation results

$$curvature = \frac{\left(\phi_y^2 * \phi_{zz} + \phi_z^2 * \phi_{yy} - 2\phi_y\phi_z\phi_{yz}\right)}{\left(\phi_y^2 + \phi_z^2\right)^{\frac{3}{2}}} \tag{10}$$

where ϕ_y and ϕ_{yy} denote the first and second-order partial derivatives of ϕ concerning y and ϕ_z and ϕ_{zz}, denote the same concerning z, which is given by

$$\phi_y^2 = \left(\frac{\partial\phi}{\partial y}\right)^2 \quad \phi_z^2 = \left(\frac{\partial\phi}{\partial z}\right)^2 \quad \phi_{yy} = \left(\frac{\partial^2\phi}{\partial y^2}\right) \quad \phi_{zz} = \left(\frac{\partial^2\phi}{\partial z^2}\right) \quad \phi_{yz} = \left(\frac{\partial^2\phi}{\partial yz}\right)$$

The Central difference approximation is given by Eq. 11.

$$\begin{aligned} \phi_y &= -\phi\left(P_l\right) + \phi\left(P_r\right) \\ \phi_z &= -\phi\left(P_d\right) + \phi\left(P_u\right) \\ \phi_{yy} &= -\phi(P_l) - 2\phi(P) + \phi(P_r) \\ \phi_{zz} &= -\phi(P_d) - 2\phi(P) + \phi(P_u) \end{aligned} \tag{11}$$

Each of the derivatives of ϕ is estimated about y and z. The value of ϕ after a small-time interval ΔT_o was approximated by the first-order Taylor expansion given by equation ϕ_t is defined by gradient descent, and ΔT_o is the time step. F_o is a force given in Eq. 12.

$$\begin{aligned} \phi((s,k), T_o + \Delta T_o) &= \Delta T_o * \phi_{T_o} + \phi((s,k), T_o) \\ \phi_{T_o} &= \alpha * curvature + \frac{F_o}{\max|F_o|} \\ \Delta T_o &= \frac{1}{(\max(\phi_t)+\varepsilon)} \end{aligned} \tag{12}$$

In Fig. 5 (a), the input image is shown. The result of the Otsu method is given in b). The proposed modified Otsu method is shown in Fig. 5(c). Segmentation by region-based active contour and segmentation by the proposed hybrid method is represented in Fig. 5(d) and (e). All the results are compared with manual expert results in Fig. 5(f).

where α is the weight of a smoothing term and ε is the coefficient to satisfy the Courant, Friedrichs, Lewy (CFL) condition [30]. A CFL condition is essential to resolve certain partial differential equations. The Sussman function (Eq. 13) [28] is used to smooth the SDF given

$$\phi_{i,j}^{M+1} = \phi_{i,j}^{M} - \Delta T_o S_\varepsilon(\phi_{i,j}) G(\phi_{i,j}^{M}) \tag{13}$$

were,

$$S_\varepsilon(\phi)_{i,j} = \frac{\phi_{i,j}^2}{\sqrt{\left(\phi_{i,j}^2\right)+\varepsilon^2}}$$

$$H\left(\phi_{i,j}^N\right) = \begin{cases} \sqrt{\left(\max\ (E^+)^2, (F^-)^2 + \max\ \left((G^+)^2,\ (H^-)^2\right)\ \right) - 1} \\ \sqrt{\left(\max\ (E^-)^2, (F^+)^2 + \max\ \left((G^-)^2,\ (H^+)^2\right)\ \right) - 1} \\ 0\ otherwise \end{cases}$$

$E^+ = max\ (E, 0)$, $E^- = min\ (E, 0)$, and so on.

The flux $G(\phi_{i,j}^M)$ is defined using the notation E, F, G, *and* H, which are the matrix that has positive and negative values. In general, the initialization of contour requires user interaction.

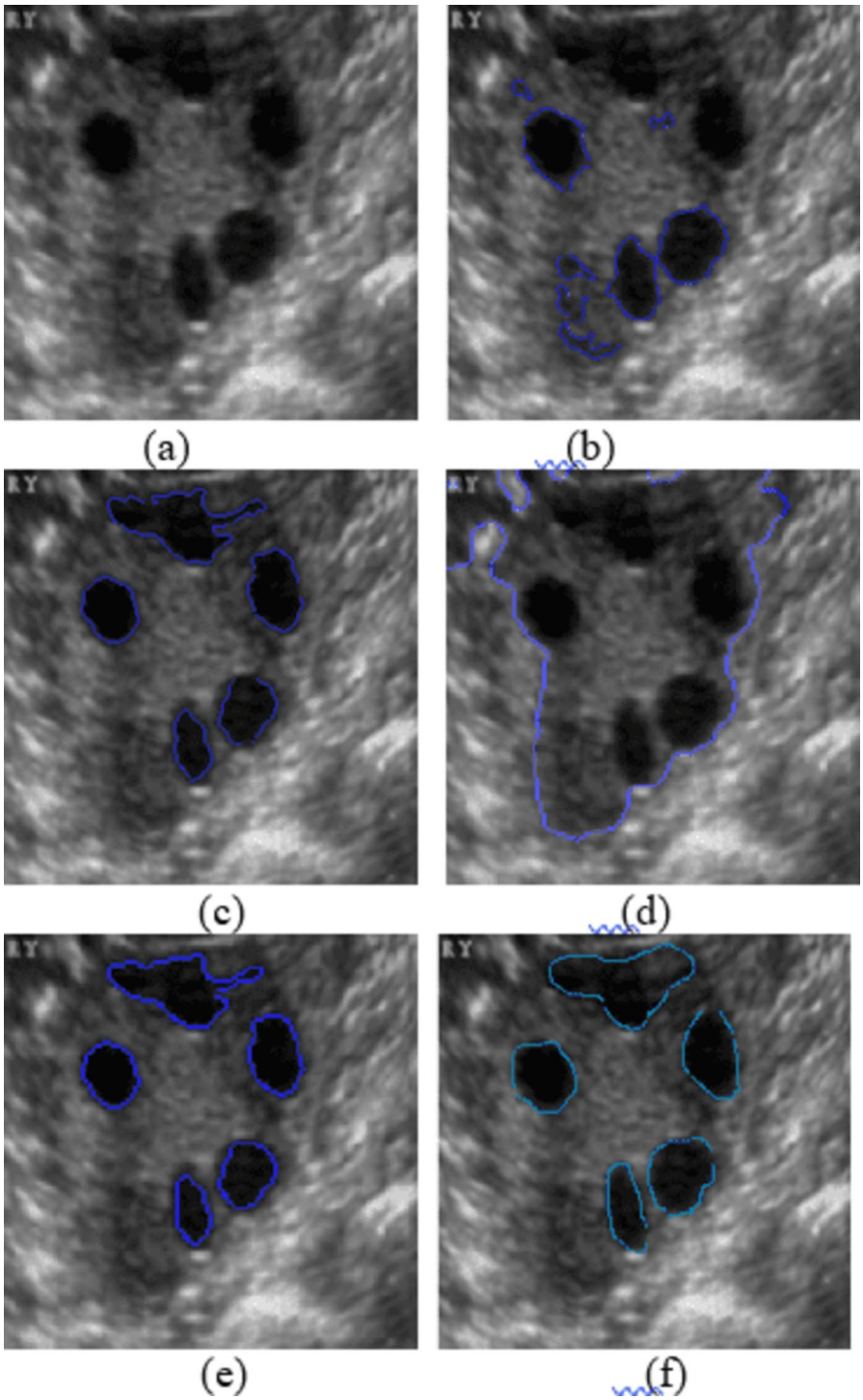

Fig. 5 Some distinctive results of the input image

In this proposed hybrid method, a fully automated technique is introduced. The results obtained from the proposed modified Otsu method are set as the initial mask. Figure 5 (c) shows the contour initialization for the Level Set method. The image is resized to segment the follicles in the ovary, the number of iterations is set as 50, and $\alpha = 0.9$ is passed as an input for region-based active contour. This technique identifies the follicle region at its 400th iteration in case of more follicles. The proposed hybrid method identified the follicular region and the edges of follicles at its 50th iteration for any ovarian image. More significantly, though the image contains more tissues than follicles, the proposed hybrid method effectively extracted the follicles from the complex background without user interaction with reduced computation time through more accuracy that matched better with prediction by human experts.

8 Feature extraction

The follicles are segmented efficiently using the proposed segmentation method. From the results, necessary feature information is extracted and measured. Feature extraction generates representative information useful for the diagnosis and classification of diseases. The shape-based parameters Area, Perimeter, Eccentricity, Major axis, Minor axis, Circularity, Extent, and Tortuosity are measured from segmented ovary images. The follicle area in an ovary image is computed as the number of pixels inside the segmented follicle. The eccentricity of a follicle is calculated by taking the proportion of the distance between the central point of the ellipse and its major axis length. The Extent varies from 0.2 to 0.7. Circularity indicates how much the follicle can deviate from a perfect circle and lies in the range of 0.2 to 0.8. Tortuosity is calculated by taking the ratio of the longest diameter of the follicle to the perimeter. It varies from 0.1 to 0.4. Based on the number and sizes of the follicles, the ovarian image is classified as normal, cystic, and polycystic. The shape-based information extracted from segmented results obtained for different methods is listed in Tables 4 and 5, and 6.

9 Classification

Classification of an ovary image into normal, cystic, and polycystic has been done based on the measured features using a Support Vector Machine (SVM). SVM is a linear classifier that effectively classifies medical images into normal and abnormal.

The SVM classifier requires a knowledge mechanism to examine through a known training set of samples. During the training phase, the image characteristics are analyzed, and the classifier organizes the data into different classes with related labels. These features are also used to classify images in the testing phase. The binary classifier can be extended to multiple-class SVM to classify images into n-classes. Based on follicle size and the number of follicles present in the ovary, the ovarian images are classified into three classes: real, cystic, and polycystic. Figure 6 is shown below.

Medical experts report that the number of follicles in a normal ovary ranges from 1 to 10 and is 2.0 to 10.0 mm in size. A cystic ovary contains 1 or 2 follicles with a size greater than 28.0 mm. The number of follicles in polycystic ovaries is 12 or more, with sizes up to 10.0 mm.

In this paper, the multiclass SVM is used for classification. Throughout the training phase, the follicle count (FC) and follicle size (FS) are computed for normal, cystic, and polycystic ovaries. The RBF kernel is used as a kernel function.

Original Image	Segmentation Methods			
	Otsu	Proposed Modified Otsu	Proposed Hybrid Method	Manual Detection
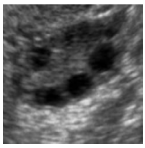				
No. of objects identified	4	6	7	7
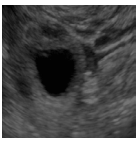				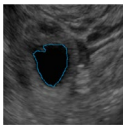
No. of objects identified	6	1	1	1
				
No. of objects identified	17	12	11	11

Fig. 6 Differences in follicle counts identified by the proposed and existing method

FC1-	Follicle count of the normal ovary
FS1-	Follicle size of the normal ovary
FC2-	Follicle count of the cystic ovary
FS2-	Follicle size of the cystic ovary
FC3-	Follicle count of the polycystic ovary
FS3-	Follicle size of the polycystic ovary

During the testing phase, the parameters follicle count (FC) and follicle size (FS) are computed to determine whether an ovary is normal, cystic, or polycystic. The classification is performed on 63 ultrasound ovary images, of which 23 images are used for training, and the remaining 40 images are used in the testing phase.

10 Experimental results

The ultrasound images of ovaries for this experimentation are collected from diagnostic centers after consultation with radiologists and gynecologists. The algorithms discussed in this paper are tested with 500 ultrasound images of ovaries captured by the GE LOGIQ ultrasound imaging system. The transvaginal probe used for capturing the image is built with an ultrasound transducer operating at a frequency of 24 MHz. The experiments have been executed on HP Pavilion dv5 with Intel® Core™ 2 Duo CPU @ 2.00 GHz with 3 GB RAM running on Microsoft Windows 7 platform. The proposed methods are implemented using Matlab 2012a software. The extensive libraries, powerful tools, and user-friendly environment of MATLAB make it important in image processing. MATLAB's Image Processing Toolbox offers various functions for image processing, analysis, visualization, and algorithm development. The toolbox offers functionality for filtering, transforming, and enhancing images as well as geometric transformations, image segmentation, and morphological operations.

MATLAB is brilliant when it comes to data visualization, as it allows one to easily display and analyze images and results. It has other capabilities, such as reading in different image formats and displaying images and histograms as pixel information. It becomes easy to understand algorithms when visualizing intermediate steps in processing, which helps debug them. For prototyping new image processing algorithms or developing them fully, a high-level programming language with an interactive environment like the one provided by MATLAB is just perfect. This speeds up the development process significantly by providing built-in functions coupled with extensive documentation, leading to quick testing and iterations by developers who are researchers or engineers. With its capability to be integrated into various software platforms, including C/C++code Java, .NET, and Python, MATLAB can take advantage of this versatility in different application contexts. Its support for integration with other software packages and hardware implies that it can accommodate MATLAB algorithms within larger systems using it together with C/C++code Java, .NET, or Python. An example of an image processing task in MATLAB is noise reduction, which uses filters like median, Gaussian, and Wiener to remove noise from images. Image Enhancement: Adjusting contrast and brightness, performing histogram equalization, and applying edge enhancement techniques. Image Segmentation: Implementing techniques such as thresholding, watershed, and region growing to segment images into meaningful regions. Object Detection: Identifying and localizing objects within images using template matching, feature-based methods, or deep learning models.

MATLAB provides various tools and functionalities, making it an excellent platform for image processing. The Image Processing Toolbox contains many algorithms and workflows for visualization, image analysis, and algorithm development. It helps users process and analyze images through its various features, such as geometric transformations, enhancement, morphological operations, or image segmentation, among others. It also supports 2D and 3D image operations, allowing for advanced tasks such as volume segmentation and 3D reconstruction. Besides this flexibility feature, MATLAB can also be integrated with other toolboxes, including the Deep Learning Toolbox or the Computer Vision Toolbox, thus expanding the frontiers of these software programs towards specialized applications like object detection or classification using machine learning models based on deep learning concepts. Therefore, researchers and engineers find this versatility quite beneficial when dealing with matters related to imaging technology. The ultrasound ovary images are classified as normal, polycystic, and cystic based on the number of follicles and size. Accurate detection of follicles results in incorrect diagnosis.

The experiments were conducted to evaluate the system's accuracy, follicle identification rate, and false acceptance rate. The images were annotated by practiced radiologists to provide ground truth data for follicle detection and ovarian classification. A total of 500 images are taken for the experiment. The total images were divided into training and testing sets. The best training and testing set ratios are 80% and 20%, respectively. So, from the dataset, 400 images are taken for training, and 100 images are taken for testing. Previously, the detection and classification of ovarian images underwent several preprocessing steps to enhance quality and ensure consistency. Therefore, various noise reduction techniques are applied to reduce speckle noise. The method's performances are evaluated using various performance metrics, and their performances are evaluated. The results show that the proposed adaptive Frost filter of 3×3 kernel size is de-noising better than all other filters used, presented in Table 2. The denoised images are taken for the segmentation process. The follicle detection algorithm was evaluated based on its ability to correctly identify and localize follicles within the ultrasound ovarian images. To substantiate the efficacy of the proposed segmentation method, a visual assessment is made of the segmented results of the Otsu method, the proposed modified Otsu method, the region-based active contour method, and the proposed hybrid method, which is shown in Figures describes a comparative study of the identified follicles by the segmentation mentioned above methods for three ultrasound ovary images. For Ovary Image 1, the Otsu method detects 4 follicles, the proposed modified Otsu method detects 6 follicles, and finally, the proposed hybrid method detects 7 follicles that exactly match with human experts' identification. The shape features are extracted from the segmented images using the Otsu method, the proposed modified Otsu method, and the hybrid method. Shape parameters considered for classification are Area, Perimeter, Major axis, Minor axis, Eccentricity, Extent, Circularity, and Tortuosity of follicles, which are calculated and listed in Tables 4 and 5, and 6. The performance metrics, including false identification and acceptance rates, were calculated to evaluate the efficiency of the proposed method. The follicle identification rate for the proposed hybrid method is 97.7%, and the false acceptance rate is 2%. The high accuracy, sensitivity, and specificity values demonstrate the system's reliability in correctly classifying ovarian conditions. To validate the effectiveness of the proposed system, its performance was compared with existing follicle detection and ovarian classification methods.

Table 7 gives the follicle identification results. It shows that the Follicle Identification Rate for the proposed hybrid method is 97.7%, and the False Acceptance Rate is 2%.

The SVM classifier is used to classify the ultrasound ovarian images into different classes. Based on the classification accuracy [48], the efficiency of the proposed method is evaluated.

Table 4 Results of feature extraction from Otsu's method

Method	Individual Follicle	Area	Perimeter	Major Axis	Minor Axis	Eccentricity	Extent	Circularity	Tortuosity
Otsu	1	1403	146.2254	47.7929	38.8989	0.5809	0.7462	0.8245	0.3268
	2	830	122.9117	39.7743	29.5237	0.6700	0.6449	0.6904	0.3236
	3	394	77.5979	26.4367	19.5553	0.6729	0.6700	0.8222	0.3406
	4	495	101.3970	42.1903	15.7462	0.9277	0.4687	0.6050	0.4160
	5	857	114.5685	35.5344	31.6657	0.4537	0.7047	0.8204	0.3101
	6	74	35.3137	14.7099	6.9835	0.8801	0.6983	0.7457	0.4165
	7	671	101.4975	33.1268	26.5182	0.5993	0.7100	0.8185	0.3263
	8	689	103.4975	31.5136	28.6852	0.4140	0.7199	0.8082	0.3044
	9	96	48.7279	20.8672	7.09851	0.9403	0.5925	0.5080	0.4282
	10	135	60.5269	25.5746	8.1232	0.9482	0.5113	0.4630	0.4225
	11	3741	417.7473	103.0747	61.3126	0.8038	0.5269	0.2693	0.2467
	12	1608	174.9949	49.3048	44.2275	0.4419	0.6434	0.6598	0.2817
	13	195	57.4558	20.1046	13.0143	0.7622	0.6632	0.7422	0.3499
	14	103	44.3847	18.2615	8.19804	0.8935	0.5722	0.6570	0.4114
	15	1901	176.0244	58.2410	42.3615	0.6862	0.7173	0.7709	0.3308
	16	83	41.5563	16.5129	7.2268	0.8991	0.6102	0.6039	0.3973
	17	528	191.8234	53.1546	26.2380	0.8696	0.6543	0.1803	0.2771
	No of Follicles Identified: 17								

Table 5 Results of feature extraction from proposed modified Otsu's method

Method	Individual Follicle	Area	Perimeter	Major Axis	Minor Axis	Eccentricity	Extent	Circularity	Tortuosity
Proposed Modified Otsu	1	1269	139.8823	45.0114	37.5171	0.5525	0.7230	0.7149	0.3217
	2	311	68.5269	23.3240	17.6308	0.6546	0.6820	0.7322	0.3403
	3	732	112.0833	37.8439	27.0226	0.7000	0.6559	0.7322	0.3376
	4	412	96.5685	39.6104	13.9217	0.9362	0.4430	0.5551	0.4001
	5	761	106.6690	32.5269	30.5955	0.3394	0.7220	0.7404	0.3049
	6	580	98.0832	30.9033	24.6577	0.6027	0.6971	0.7576	0.3150
	7	589	92.4264	29.5845	26.0111	0.4764	0.7307	0.7664	0.3200
	8	1767	255.0366	70.9228	34.6200	0.8727	0.4867	0.3413	0.2780
	9	1417	150.7107	47.0169	39.9255	0.5281	0.7353	0.7839	0.3119
	10	1000	189.4386	44.7331	33.0268	0.6744	0.5050	0.3501	0.2361
	11	1759	171.6812	55.8660	40.9404	0.6804	0.7038	0.7499	0.3254
	12	52	27.8994	9.7820	7.6236	0.6265	0.6419	0.8395	0.3506
	No of Follicles Identified: 12								

Table 6 Results of feature extraction from proposed hybrid method

Method	Individual Follicle	Area	Perimeter	Major Axis	Minor Axis	Eccentricity	Extent	Circularity	Tortuosity
Proposed Hybrid Method	1	316	66.2842	22.5176	18.5406	0.5674	0.7559	0.7038	0.3397
	2	74	29.8994	11.4336	8.4547	0.6731	0.8009	0.7040	0.3824
	3	176	51.2132	18.2017	13.3194	0.6815	0.6901	0.8432	0.3554
	4	97	40.6274	18.3712	6.9437	0.9258	0.5329	0.7384	0.4521
	5	185	49.2132	15.9711	15.0886	0.3278	0.7708	0.7598	0.3245
	6	142	44.6274	15.1518	12.2587	0.5877	0.7395	0.7959	0.3395
	7	143	42.9705	14.6643	12.7131	0.4983	0.7944	0.7732	0.3412
	8	435	104.0833	34.9467	17.0111	0.8735	0.5409	0.5114	0.3372
	9	353	70.2842	23.3807	19.8720	0.5268	0.7652	0.7954	0.3330
	10	242	74.8700	21.7270	15.8405	0.6844	0.5487	0.5425	0.2901
	11	436	79.1127	27.8337	20.2830	0.6848	0.7582	0.6753	0.3518
	No of Follicles Identified: 11								

10.1 Accuracy range classification

0.9 > Excellent.
0.8 > and < 0.9 Good.
0.7 > and < 0.8 Valueless.
0.6 > and < 0.7 Not good.

The obtained results of the proposed and existing methods are presented in Table 8.

The results show that the proposed hybrid method yields more accurate results than other methods. The classification accuracy of the proposed method is 98.3%.

From the experimental results, as consolidated in the comparison chart of Fig. 7, it can be observed that the proposed algorithm is an improvement over existing algorithms and matches more accurately with the assessment by medical experts. The Otsu method classifies the Ovary Image2 as normal from the extracted features. However, the proposed automatic diagnostic system classifies Ovary Image 1 as a normal ovary, Ovary Image 2 as a cystic ovary, and Ovary Image 3 as a polycystic ovary. The result matches the medical experts' results. Thus, it argues for the implementation of a more accurate and efficient automatic detection algorithm for identifying PCOS in ultrasound ovary images.

11 Limitations

However, the design of this automatic follicle detection and ovarian classification system for ultrasound ovarian images has several shortcomings despite these promising results. The success of diagnostic systems on input images is influenced by the quality of ultrasound images used as input. Inconsistencies in image quality may result from differences in parameters during image acquisition, operator skill level, and patient conditions, which

Table 7 Comparision of the SVM with the human experts' identification of follicles

No Ovarian Images	Follicles detected by the proposed hybrid method	Follicles detected by human experts	Follicle Identification Rate (%)	False Acceptance Rate (%)
500	785	779	97.7%	2%

Table 8 Comparison of the proposed method with the existing method

Metric	Proposed method	Modified Otsu method	Otsu Method
Follicle Detection rate	97.7%	90.4%	77.4%
PCOS Classification Accuracy	98.3%	91.2%	68.8%

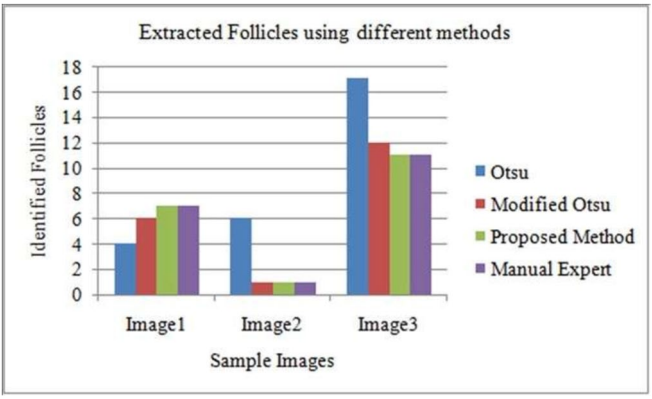

Fig. 7 Comparison chart for identified follicles

may also affect the accuracy of preprocessing and segmentation stages. Nevertheless, there still are some remaining noises after applying the adaptive Frost filter, which might affect the segmentation process, leading to false detection in follicles. Moreover, when it comes to more severe polycystic cases, where there is a chance that a few closely located or even overlapping follicles are present, this can be difficult for the region-based active contour technique combined with a modified Otsu algorithm. The adaptability of this system to different imaging situations is also hampered by its dependence on some specific parameter settings for noise reduction and segmentation alone.

12 Conclusion

This study introduced a computationally efficient system for the automatic and accurate detection of follicles in ultrasound ovarian images. The adaptive Frost filter effectively denoises the ultrasound images, which are then processed by the proposed segmentation algorithm to identify follicles. Features extracted from these segmented follicles are used as input parameters for the SVM classifier. The proposed hybrid method achieves a Follicle Identification Rate of 97.7% and a False Acceptance Rate of 2%. The results demonstrate that this hybrid method offers a higher accuracy rate than other techniques, achieving 98.3% accuracy. Thus, the proposed system is a cost-effective and efficient tool that can assist radiologists and gynecologists in studying menstrual cycles and diagnosing patients undergoing infertility treatment.

Appendix

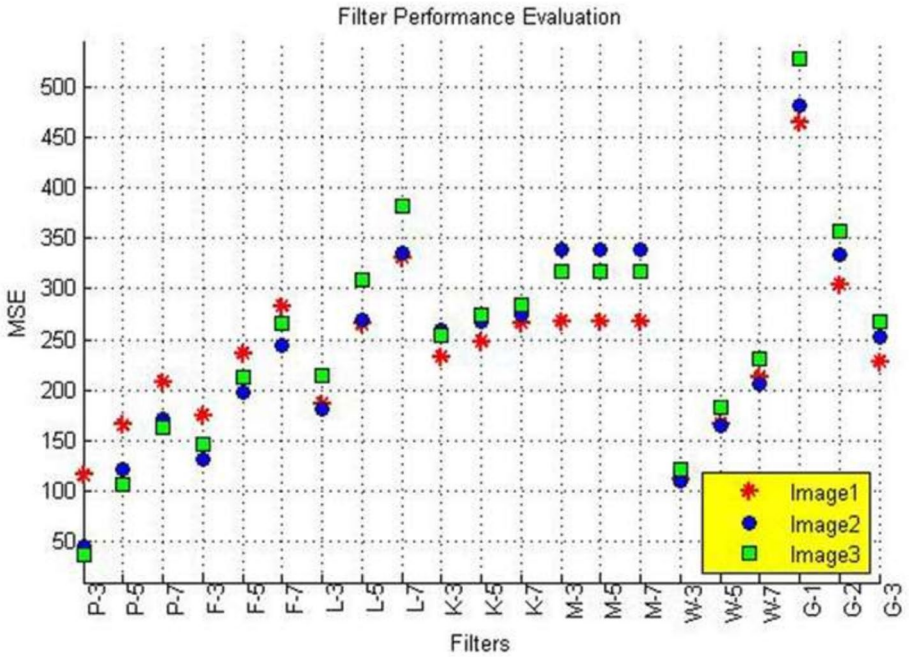

Fig A1 Filter performance graph for Mean Square Error

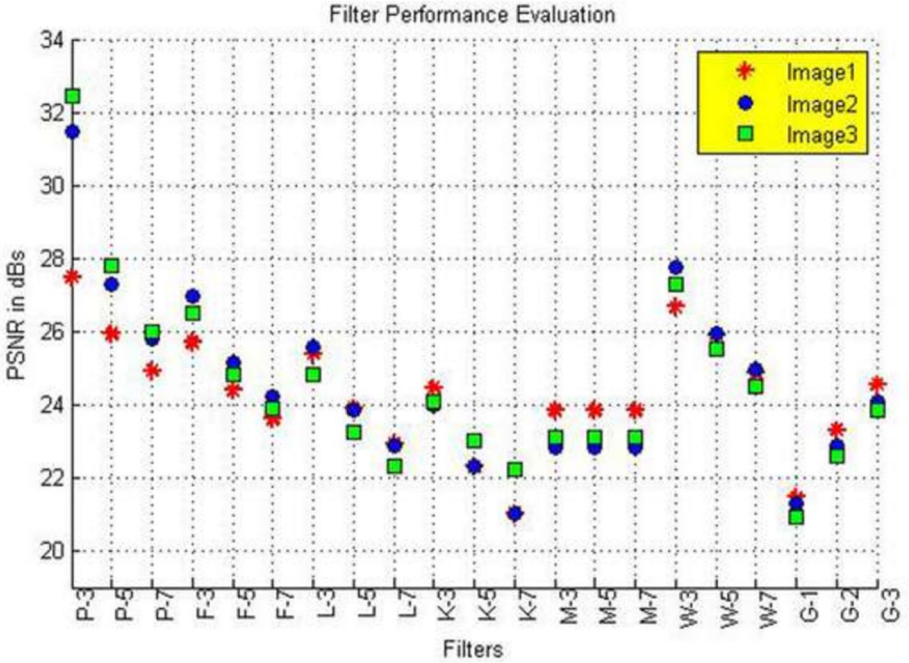

Fig. A2 Filter performance graph for Peak Signal Noise Ratio

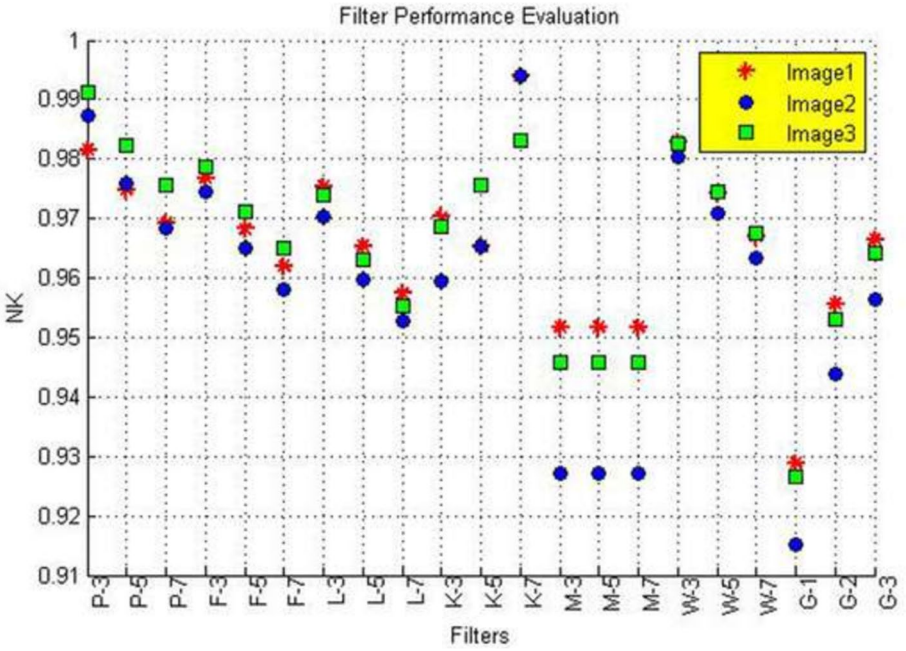

Fig. A3 Filter performance graph for Normalized cross-correlation

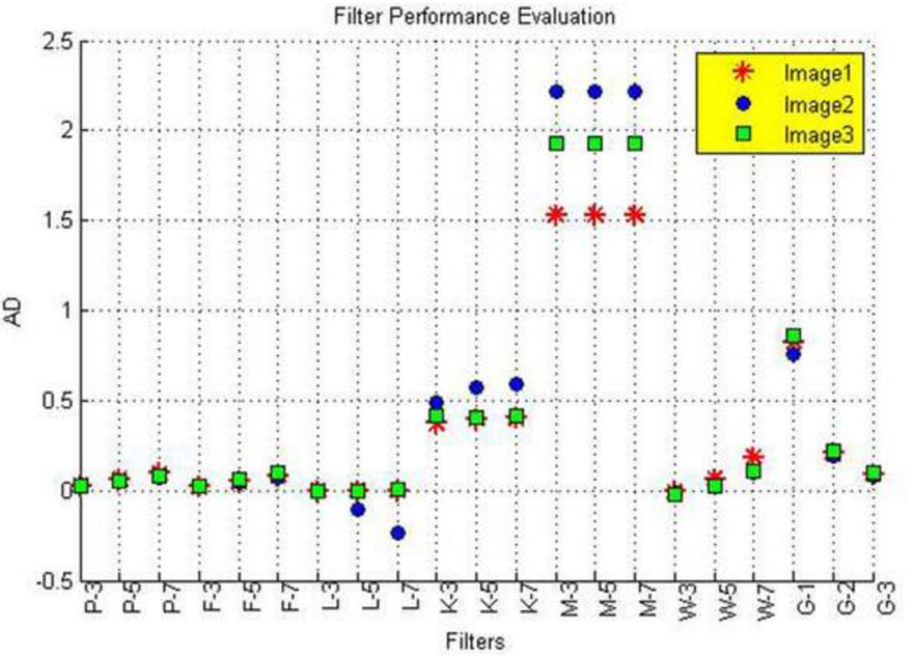

Fig. A4 Filter performance graph for Absolute Difference

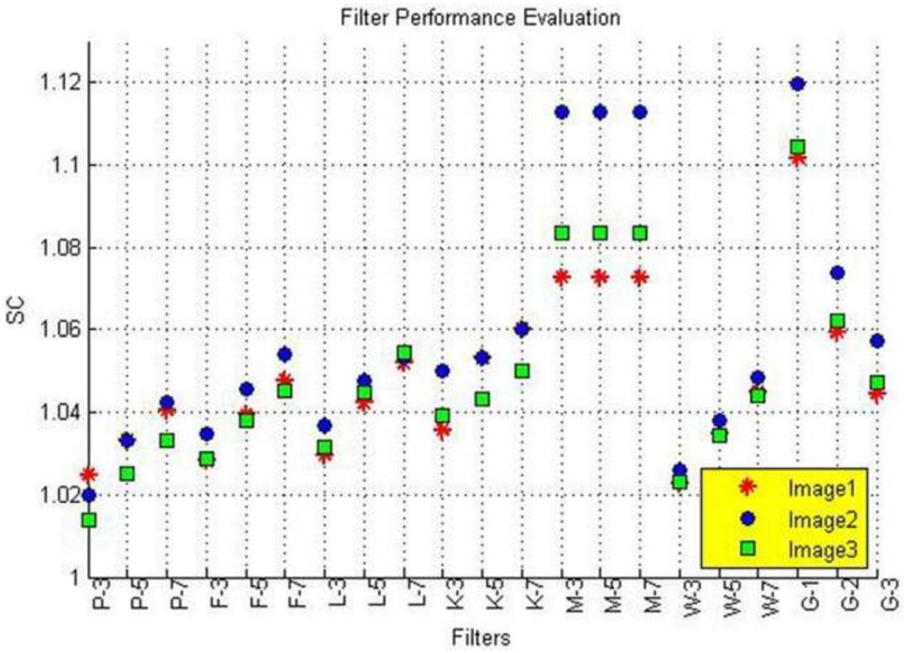

Fig. A5 Filter performance graph for Structural Content

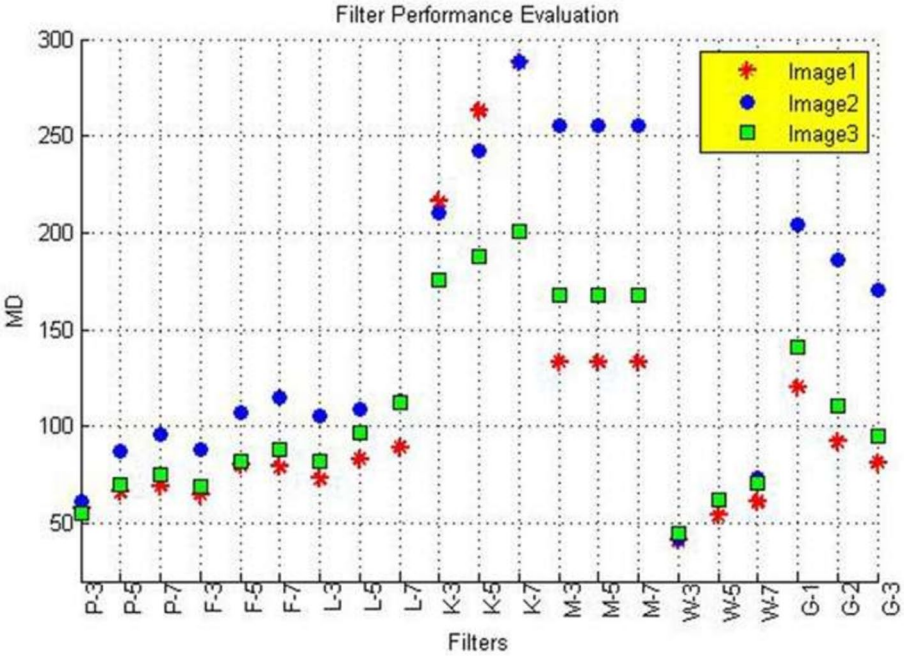

Fig. A6 Filter performance graph for Maximum Difference

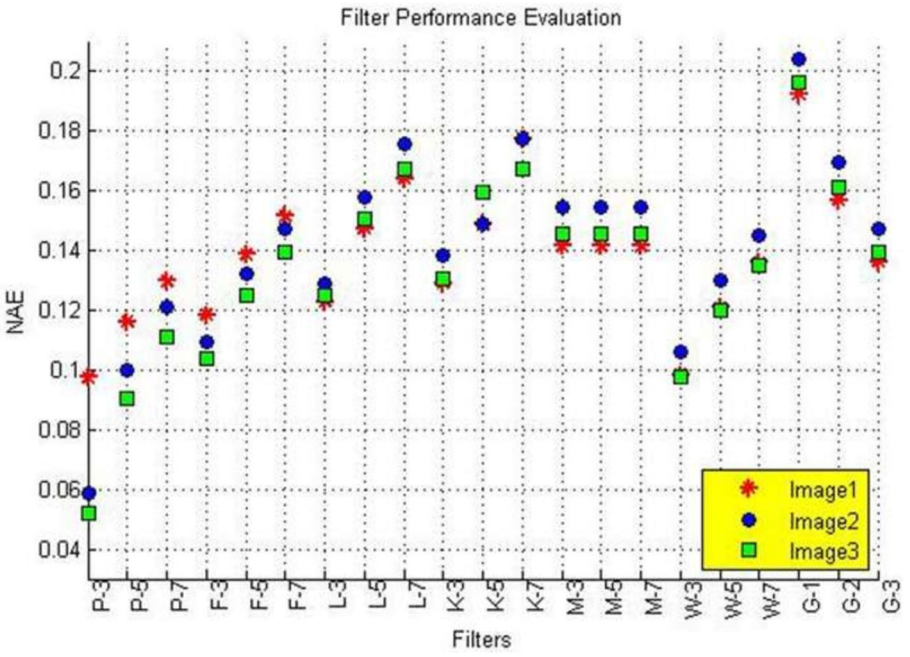

Fig. A7 Filter performance graph for Normalized Absolute Error

Abbreviations AD: Absolute Difference; FC: Follicle count; FS: Follicle size; MSE: Mean Square Error; MD: Maximum Difference; NK: Normalized Cross-Correlation; NAE: Normalized Absolute Error; PCOS: Polycystic Ovarian Syndrome; PSNR: Peak Signal to Noise Ratio; ROI: Region of Interest; SC: Structural Content; SVM: Support Vector Machine

Data availability All the data is collected from the simulation reports of the software and tools used by the authors. The authors are working on implementing them using real-world data with appropriate permissions.

Declarations

Conflict of interest The authors declare that we have no conflict of interest.

References

1. The Lancet (n.d.) Polycystic Ovary Syndrome: 1 In 15 women affected worldwide and burden likely to increase. ScienceDaily. www.sciencedaily.com/releases/2007/08/070831204314.htm. Accessed 26 Nov 2014
2. Jokubkiene L, Sladkevicius P, Valentin L (2012) Ovarian size and vascularization as assessed by three-dimensional grayscale and power Doppler ultrasound in asymptomatic women 20–39 years old using combined oral contraceptives. Contraception 86(3):257–267
3. Jokubkiene L, Sladkevicius P, Valentin L (2012) Number of Antral Follicles, ovarian volume, and vascular indices in asymptomatic women 20 to 39 years old as assessed by 3-dimensional sonography. J Ultrasound Med 31(10):1635–1649

4. Yamanaka Y, Tateiwa Y (2005) Preoperative diagnosis of malignant transformation in mature cystic teratoma of the ovary. Eur J Gynaecol Oncol 26(4):391–392
5. Balen Adam SE, Joop L, Tan S-L, Dewailly D (2003) Ultrasound Assessment of the Polycystic Ovary: International Consensus Definitions. Hum Reprod 9(6):505–514
6. RaineFenning N, Jayaprakasan K, Clewes J (2007) Automated follicle tracking facilitates standardization and may improve work flow. Ultrasound Obstet Gynecol 30(7):1015–1018
7. Battaglia C, Artini PG, Genazzani AD, Gremigni R, Slavatori MR, Sgherzi MR (1997) Color doppler analysis in oligo and amenorrheic women with polycystic ovary syndrome. Gynaecol Endocrinol 11(2):105–110
8. Bal A, Mohan H, Singh SB, Sehgal A (2007) Malignant transformation in mature cystic teratoma of the ovary: report of five cases and review of the literature. Arch Gynecol Obstet 275(3):179–182
9. Aysal TC, Barner KE (2007) Rayleigh-maximum-likehood filtering for speckle reduction of ultrasound images. IEEE Trans Med Imaging 26(5):712–727
10. Mencattini A, Salmeri M, Lojacono R, Frigerio M, Caselli F (2008) Mammographic images enhancement and denoising for breast cancer detection using dyadic wavelet processing. IEEE Trans Instrum Meas 57(7):1422–1430
11. Firoiu Ioana, Corina Nafornita J-M, Boucher AlexandruIsar (2009) Image denoising using a new implementation of the hyperanalytic wavelet transform. IEEE Trans Instrum Meas 58(8):2410–2416
12. Russo F (2007) An image-enhancement system based on noise estimation. IEEE Trans Instrum Meas 56(4):1435–1442
13. Gifani P, Behnam H, Sani ZA (2014) Noise reduction of echocardiographic images based on temporal information. IEEE Trans Ultrason Ferroelectr Freq Control 61(4):620–630
14. Michailovich OV, Tannenbaum A (2006) Despeckling of Medical Ultrasound Images. IEEE Trans Ultrason Ferroelectr Freq Control 53(1):64–78
15. Sforza G, Castellano G, Arika SA, LeAnder RW, Stanley RJ, Stoecker WV, Hagerty JR (2012) Using adaptive thresholding and skewness correction to detect gray areas in melanoma in situ images. IEEE Trans Instrum Meas 61(7):1839–1847
16. Delsanto S, Molinari F, Giustetto P, Liboni W, Badalamenti S, Suri JS (2007) Characterization of a completely user-independent algorithm for carotid artery segmentation in 2-D ultrasound images. IEEE Trans Instrum Meas 56(4):1265–1274
17. Gao H, Wenbo X, Sun J, Tang Y (2010) Multilevel thresholding for image segmentation through an improved quantum-behaved particle swarm algorithm. IEEE Trans Instrum Meas 59(4):934–946
18. Deng Y, Wang Y, Shen Y (2011) An automated diagnostic system of polycystic ovary syndrome based on object growing. J Med Artif Intell 51(3):199–209
19. Soloperto G, Conversano F, Greco A, Casciaro E, Ragusa A, Leporatti S, Lay-Ekuakille A, Casciaro S (2014) multiparametric evaluation of the acoustic behavior of halloysite nanotubes for medical echographic image enhancement. IEEE Trans Instrum Meas 63(6):1423–1430
20. Bhateja V, Misra M, Urooj S, Lay-Ekuakille A (2013) A Robust Polynomial Filtering Framework for Mammographic Image Enhancement from Biomedical Sensors. IEEE Sens J 13(11):4147–4156
21. Chiriaco F, Conversano F, Sbenaglia EA, Casciaro S, Lay-Ekuakille A (2014) Cytotoxicity, "measurements of halloysite nanotubes for nanomedicine applications". IEEE MeMea, Lisbon, Portugal pp. 11–12
22. Giordano D, Spampinato C, Scarciofalo G, Leonardi R (2010) An automatic system for skeletal bone age measurement by robust processing of carpal and epiphysial/metaphysial bones. IEEE Trans Instrum Meas 59(1):2539–2553
23. Berahmand K, Daneshfar F, Salehi ES et al (2024) Autoencoders and their applications in machine learning: a survey. Artif Intell Rev 57:28. https://doi.org/10.1007/s10462-023-10662-6
24. Sajjad Amiri Doumari, Kamal Berahmand, M J Ebadi (2023) Early and high-accuracy diagnosis of Parkinson's disease: outcomes of a new model. Comput. Math. Methods Med. https://doi.org/10.1155/2023/1493676
25. Chan T, Vese L (2001) Active contours without edges. IEEE Trans on Image Process 10(2):266–277
26. Finn S, Glavin M, Jones E (2011) Echocardiographic speckle reduction comparision. IEEE Trans Ultrason Ferroelectr Freq Control 58(1):82–101
27. Kanaka Rajan P, Harvey CD, Tank DW (2021) An Enhanced Adaptive Histogram Equalization Based Local Contrast Preserving Technique for HDR Images. IOP Conf Ser: Mater Sci Eng 1022(1):012119. https://doi.org/10.1088/1757-899X/1022/1/012119
28. Brahim PA, Górriz JM, Ramírez J, Khedher L (2015) Intensity normalization of Datascan spect imaging using a model-based clustering approach. Appl Soft Comput 37:234–244
29. Wang et al (2013) Deep-tissue photoacoustic tomography of Forster resonance energy transfer. J Biomed Opt 18(10):101316

30. Petroudi S, Loizou C, Pantziaris M, Pattichis C (2012) Segmentation of the common carotid intima-media complex in ultrasound images using active contours. IEEE Trans Biomed Eng 59(11):3060–3069
31. Linguraru MG, Richbourg WJ, Liu J, Watt JM, Pamulapati V, Wang S, Summers RM (2012) Tumor Burden analysis on computed tomography by automated liver and tumor segmentation. IEEE Trans on Image Process 31(10):1965–1976
32. Cai H, Yang Z, Cao X, Xia W, Xiaoyin Xu (2014) A new iterative triclass thresholding technique in image segmentation. IEEE Trans on Image Process 23(3):1038–1045
33. Ronneberger O, Fischer P, Brox T (2015) U-Net: convolutional networks for biomedical image segmentation. In International conference on medical image computing and computer-assisted intervention (pp. 234-241). Springer, Cham
34. Çiçek Ö, Abdulkadir A, Lienkamp SS, Brox T, Ronneberger O (2016) 3D U-Net: learning dense volumetric segmentation from sparse annotation. In International conference on medical image computing and computer-assisted intervention (pp. 424-432). Springer, Cham
35. Oktay O, Schlemper J, Folgoc LL, Lee MCH, Heinrich MP, Misawa K, Mori K, McDonagh SG, Hammerla NY, Kainz B, Glocker B, Rueckert D (2018) Attention U-Net: Learning where to look for the pancreas. arXiv preprint arXiv:1804.03999
36. Chen LC, Papandreou G, Kokkinos I, Murphy K, Yuille AL (2018) DeepLab: Semantic image segmentation with deep convolutional nets, atrous convolution, and fully connected CRFs. IEEE Trans Pattern Anal Mach Intell 40(4):834–848
37. Chen LC, Zhu Y, Papandreou G, Schroff F, Adam H (2018) Encoder-decoder with atrous separable convolution for semantic image segmentation. In Proceedings of the European conference on computer vision (ECCV), pp. 801-818
38. Zhang H, Dana K, Shi J, Zhang Z, Wang X, Tyagi A, Agrawal A, Huang T (2018) Context encoding for semantic segmentation. In Proceedings of the IEEE conference on computer vision and pattern recognition (CVPR), pp. 7151–7160
39. Fu J, Liu J, Tian H, Li Y, Bao Y, Fang Z, Lu H (2019) Dual attention network for scene segmentation. In Proceedings of the IEEE conference on computer vision and pattern recognition (CVPR), pp. 3146-3154
40. Zhao H, Shi J, Qi X, Wang X, Jia J (2017) Pyramid scene parsing network. In Proceedings of the ieee conference on computer vision and pattern recognition (CVPR), pp. 2881–2890
41. Milletari F, Navab N and Ahmadi SA(2016) V-Net: Fully convolutional neural networks for volumetric medical image segmentation. In Proceedings of the IEEE conference on 3D vision (3DV), pp. 565-571
42. Isensee F, Petersen J, Klein A, Zimmerer D, Jaeger PF, Kohl S, Wasserthal J, Koehler T, Norajitra T, Wirkert S, Maier-Hein KH, Maier-Hein L (2018) nnU-Net: self-adapting framework for U-Net-based medical image segmentation. Nat Methods 18(2):203–211
43. Hesamian MH, Jia W, He X, Kennedy P (2019) Deep learning techniques for medical image segmentation: Achievements and challenges. J Digit Imaging 32(4):582–596
44. Li X, Chen H, Qi X, Dou Q, Fu CW, Heng PA (2019) H-DenseUNet: Hybrid densely connected UNet for liver and tumor segmentation from CT volumes. IEEE Trans Med Imaging 38(5):2439–2449
45. Dou Q, Yu L, Chen H, Jin Y, Yang X, Qin J, Heng PA (2017) 3D deeply supervised network for automated segmentation of volumetric medical images. Med Image Anal 41:40–54
46. Baumgartner CF, Kamnitsas K, Matthew J, Fletcher TP, Smith S, Koch LM, Kainz B, Williams M, Kaden E, Rueckert D (2017) Visual interpretation of deep learning models for brain tumor segmentation. arXiv preprint arXiv:1708.00589
47. Wang G, Li W, Ourselin S, Vercauteren T (2019) Automatic brain tumor segmentation using cascaded anisotropic convolutional neural networks. Brainlesion: Glioma Multiple Sclerosis, Stroke, and Traumatic Brain Inj 11384:178–190
48. Zhu W, Zeng N, Wang N (2010) Sensitivity, specificity, accuracy, associated confidence interval and roc analysis with practical SAS Implementations. Health Care and Life Sciences, Washington, PA, Octagon Research Solutions, Wayne, PA, pp 1-9

Publisher's Note Springer Nature remains neutral with regard to jurisdictional claims in published maps and institutional affiliations.

Springer Nature or its licensor (e.g. a society or other partner) holds exclusive rights to this article under a publishing agreement with the author(s) or other rightsholder(s); author self-archiving of the accepted manuscript version of this article is solely governed by the terms of such publishing agreement and applicable law.